

Chandra Observations of the Disruption of the Cool Core in Abell 133

Yutaka Fujita^{1,2}, Craig L. Sarazin², Joshua C. Kempner², L. Rudnick³, O. B. Slee⁴ A. L. Roy⁵, H. Andernach⁶, and M. Ehle^{7,8}

ABSTRACT

We present the analysis of a *Chandra* observation of the galaxy cluster Abell 133, which has a cooling flow core, a central radio source, and a diffuse, filamentary radio source which has been classified as a radio relic. The X-ray image shows that the core has a complex structure. The most prominent feature is a “tongue” of emission which extends from the central cD galaxy to the northwest and partly overlaps the radio relic. Spectral analysis shows that the emission from the tongue is thermal emission from relatively cool gas at a temperature of ~ 1.3 keV. One possibility is that this tongue is produced by Kelvin-Helmholtz (KH) instabilities through the interaction between the cold gas around the cD galaxy and hot intracluster medium. We estimate the critical velocity and time scale for the KH instability to be effective for the cold core around the cD galaxy. We find that the KH instability can disrupt the cold core if the relative velocity is $\gtrsim 400$ km s⁻¹. We compare the results with those of clusters in which sharp, undisrupted cold fronts have been observed; in these clusters, the low temperature gas in their central regions has a more regular distribution. In contrast

¹National Astronomical Observatory, Osawa 2-21-1, Mitaka, Tokyo 181-8588, Japan; yfujita@th.nao.ac.jp

²Department of Astronomy, University of Virginia, P.O. Box 3818, Charlottesville, VA 22903-0818, USA; sarazin@virginia.edu, jck7k@virginia.edu

³Department of Astronomy, University of Minnesota, 116 Church Street SE, Minneapolis, MN 55455

⁴Australia Telescope National Facility, CSIRO, PO Box 76, Epping, NSW 1710, Australia

⁵Max-Planck-Institut für Radioastronomie, Auf dem Hügel 69, D-53121 Bonn, Germany

⁶Depto. de Astronomía, Univ. Guanajuato, Apdo. Postal 144, Guanajuato, C.P. 36000, GTO, Mexico

⁷XMM-Newton Science Operations Centre, Apartado 50727, E-28080 Madrid, Spain

⁸Science Operations & Data Systems Division, Research and Scientific Support Department of ESA, ESTEC, 2200 AG Noordwijk, The Netherlands

to Abell 133, these cluster cores have longer timescales for the disruption of the core by the KH instability when they are normalized to the timescale of the cD galaxy motion. Thus, the other cores are less vulnerable to KH instability. Another possible origin of the tongue is that it is gas which has been uplifted by a buoyant bubble of nonthermal plasma that we identify with the observed radio relic. From the position of the bubble and the radio estimate of the age of the relic source, we estimate a velocity of $\sim 700 \text{ km s}^{-1}$ for the bubble. The structure of the bubble and this velocity are consistent with numerical models for such buoyant bubbles. The energy dissipated by the moving bubble may affect the cooling flow in Abell 133. The combination of the radio and X-ray observations of the radio relic suggest that it is a relic radio lobe formerly energized by the central cD, rather than a merger-shock generated cluster radio relic. The lobe may have been displaced from the central cD galaxy by the motion of the cD galaxy or by the buoyancy of the lobe.

Subject headings: galaxies: clusters: general — galaxies: clusters: individual (Abell 133) — cooling flows — intergalactic medium — radio continuum: galaxies — X-rays: galaxies: clusters

1. Introduction

The advent of the *Chandra X-ray Observatory* enables us to study the intracluster medium (ICM) in clusters of galaxies with superb spatial resolution. *Chandra* has revealed the dynamics of substructures in the central region of clusters. In some clusters, sharp contact surfaces between the cold gas in merging subcluster cores and the hot ICM have been observed (Markevitch et al. 2000; Vikhlinin, Markevitch, & Murray 2001b; Mazzotta et al. 2001). These contact surfaces are often called ‘cold fronts’. They are interpreted as cool cores from subclusters which are moving through the main body of the cluster without losing their identity (Markevitch et al. 2000; Vikhlinin et al. 2001b; Mazzotta et al. 2001). The existence of those cold fronts also provides information about fluid dynamics, transport properties, and magnetic fields in the ICM. Vikhlinin, Markevitch, & Murray (2001a) argued that magnetic fields provide a surface tension that stabilizes the cold fronts against the development of Kelvin-Helmholtz (KH) instabilities. *Chandra* has also provided more detailed information on cluster merger shocks than the previous observations with *ROSAT* and *ASCA* (e.g., Henry & Briel 1995; Markevitch, Sarazin, & Vikhlinin 1999; Furusho et al. 2001). For Abell 665, Markevitch & Vikhlinin (2001) showed that radio emission comes from high temperature shock regions; this suggests that relativistic electrons are accelerated in merger shocks.

Another important result from *Chandra* is the discovery of complex X-ray structures in the central regions of cooling flow clusters with radio sources. Recent *Chandra* images and earlier results from *ROSAT* show that central radio sources in cooling flow clusters can inflate bubbles of nonthermal plasma which displace the X-ray emitting gas (Böhringer et al. 1993; Carilli, Perley, & Harris 1994; Huang & Sarazin 1998; Fabian et al. 2000; McNamara et al. 2000; Blanton et al. 2001; Mazzotta et al. 2002a). The X-ray images of the central regions of the Hydra A and Perseus clusters revealed minima in the X-ray emission coincident with the radio lobes (McNamara et al. 2000; Fabian et al. 2000). Subsequently, similar X-ray minima, corresponding to radio bubbles, were found in Abell 2052 and MKW3s (Blanton et al. 2001; Mazzotta et al. 2002a); a particularly strong interaction between the ICM and radio plasma was found in Abell 2052 (Blanton et al. 2001). For Hydra A, David et al. (2001) suggested that the AGN activity may prevent the gas from cooling to low temperatures (see also Ikebe et al. 1997). This suggests that these central regions are not simple, spherically-symmetric, hydrostatic systems. A wealth of previous X-ray observations has shown that gas in the cores of many clusters is cooling through at least part of the X-ray emitting temperature range from $\sim 10^8$ to $\sim 10^7$ K (see Fabian 1994, for a review). Since the cooling time of gas in many cluster cores is well below the age of the Universe, cooling flows are the natural consequence of radiative cooling if there are no balancing heat sources. More recent spectral observations suggest that the gas does not continue to cool down to low temperatures at the rates suggested previously (Peterson et al. 2001). Previous *ASCA* observations had also suggested this (see Makishima et al. 2001, for a review).

Abell 133 is an X-ray luminous cluster at $z = 0.0562$ (Way, Quintana, & Infante 1997) with a central cooling flow (White, Jones, & Forman 1997). The central cD galaxy is a radio source (Slee & Reynolds 1984). There also is a diffuse, very steep spectrum radio source ~ 30 kpc north of the center of the cD galaxy, which has no optical counterpart and is classified as a radio relic (Slee et al. 2001). The radio relic source has an unusual filamentary structure. A comparison of previous *ROSAT* X-ray and *VLA* radio observations revealed an excess of X-ray emission near the cluster center which was spatially coincident with the radio relic (Rizza et al. 2000; Slee et al. 2001). Rizza et al. (2000) argued that the enhanced emission was the result of the interaction between a jet from the cD nucleus with hot ICM. Slee et al. (2001) indicated that the excess X-ray emission in the 0.5 – 2.0 keV band is too high to be attributed to the inverse Compton (IC) emission from the high energy particles in the relic alone. On the basis of *ROSAT* data alone, one cannot draw a conclusion about the interaction between the radio plasma and the hot ICM because of *ROSAT*'s limited spatial resolution and bandwidth. In this paper, we present *Chandra* observations of the central region of Abell 133, which we use to study the X-ray morphology, temperature distribution, and the contribution of nonthermal emission. We assume $H_0 = 70 \text{ km s}^{-1} \text{ Mpc}^{-1}$, $\Omega_0 = 0.3$,

and $\Omega_\Lambda = 0.7$ unless otherwise mentioned. At a redshift of 0.0562, $1''$ corresponds to 1.07 kpc.

2. Spatial Structure

2.1. X-ray Images

Abell 133 was observed with *Chandra* on 2000 October 13–14 for a useful exposure time of 35.5 ks. The observation was made with the center of the cluster located between node boundaries near the aim point on the back-illuminated chip S3. The detector temperature during the observation was -120 C. Hot pixels, bad columns, and events with grades 1, 5, and 7 were excluded from the analysis. A few periods of time containing background flares were removed using the LC_CLEAN software provided by Maxim Markevitch⁹. Only data from the S3 chip are discussed here.

Figure 1a shows the raw *Chandra* image of the inner $2' \times 2'$ region of the cluster in the 0.3 – 10 keV energy band, uncorrected for exposure or background. Figure 1b shows an adaptively smoothed image of the same region. The *Chandra* Interactive Analysis of Observation (CIAO¹⁰ 2.0) routine CSMOOTH was used. The image has a minimum signal-to-noise ratio of three per smoothing beam and was corrected for exposure, vignetting, and background. The background was taken from blank sky observations compiled by Maxim Markevitch⁸. Complex X-ray structures are seen within $\sim 1'$ of the center of the cluster. The most prominent is a “tongue”-like feature which extends from the cluster center to the northwest, and ends in two knots of emission. This tongue can be identified with the excess X-ray emission feature observed by *ROSAT* (Fig. 1b in Rizza et al. 2000 and Fig. 12b in Slee et al. 2001). To either side of the tongue, the X-ray surface brightness is rather low. At the southeast edge of the faint region to the east of the tongue, there is a diffuse arc of brighter X-ray emission which curves toward the northeast. The core region appears to have a relatively sharp, curved edge to the southeast.

Within the core region, there are several bright knots of X-ray emission, as well as the two knots at the end of the tongue. Several of these knots appear to be small enough to be due to unresolved point sources. We used the wavelet source detection method to detect possible point sources in the image. The CIAO WAVDETECT⁹ routine was used with the significance threshold set at 1×10^{-6} . Within the central region of the cluster, three sources

⁹See <http://asc.harvard.edu/cal/Links/Acis/acis/Cal.prods/bkgrnd/current/index.html>.

¹⁰See <http://asc.harvard.edu/ciao/>.

were detected with sizes consistent with point sources; they are indicated in Figure 2. Source C is the western knot at the tip of the tongue of X-ray emission.

In Figure 3, the 1.4 GHz radio image from Slee et al. (2001) is shown in green, superposed on the adaptively smoothed *Chandra* X-ray image (Figure 1b) in red. Contours from the radio image are also shown in Figure 2. A fairly compact radio source is associated with the central cD galaxy. This appears in yellow in Figure 3 as this is also a peak in the X-ray image. This figure also shows the extended filamentary radio relic source to the NNW. The bright knots at the tip of the X-ray tongue are projected on the radio relic source, to the west of the brightest portion, and the yellow-orange color indicates that this region is bright in both radio and X-rays. However, most of the radio relic lies to the east and west of the tongue, projected on regions of relatively low X-ray surface brightness. An interesting aspect of the radio image are the long filaments extending to the east and south-east of the main portion of the relic. These filaments appear to wrap around the “wing” of brighter X-ray emission in this direction. Also, there is some evidence that a shorter radio filament wraps around the northern edge of the tip of the X-ray tongue.

In Figure 4, the X-ray contour plot of the central region of Abell 133 is overlaid on the optical Digital Sky Survey (DSS) image. As can be seen, there is no optical counterpart of the X-ray tongue, neither for the entire tongue, nor for the point-like knots (including source C) at the end of the tongue. X-ray source B corresponds to a galaxy (2MASXi J0102379–215305); the optical position agrees with the X-ray position to within $1''$ and the galaxy is a member of Abell 133 (Way et al. 1997). This galaxy is also a compact radio source (Slee et al. 2001). The X-ray source A is close to the optical center of the cD galaxy and the core of the central radio source in the cD galaxy, but is separated by about $3''$ to the south. It is not clear whether source A is really a distinct point source, perhaps due to the radio active galactic nucleus (AGN) of the cD galaxy, or whether it is just the peak in the cluster surface brightness profile. The position of the cD galaxy, central radio source, and central X-ray peak are all shifted from the larger scale center (see §2.2) of the X-ray emission toward the south.

To help visualize the faint X-ray structures around the cD galaxy, we compare the observed cluster to a smooth elliptical isophotal model. Elliptical isophotes are fitted to the image using the IRAF/STSDAS task ELLIPSE. Before the fitting, we smoothed the image with a Gaussian kernel with a width of $1''$. Since the X-ray structure around the cD is very complicated, the ellipticity, position angle, centroid, and intensity of the elliptical isophotes are all allowed to vary, except that the centroid of the innermost elliptical isophote is fixed to the position of the cD galaxy. The fits to the elliptical isophotes are used to create a smooth model of the image, which is subtracted from the original X-ray image of

the cluster. The counts of the model image are multiplied by 0.5 before the subtraction to avoid oversubtraction. Figure 5 shows the subtracted image of the cluster. The cluster is nearly axisymmetric about the tongue; faint wings extend from the center to the NE and SW. This “bird-like” structure and the shift of the cD galaxy toward the south or southwest may indicate that the cD galaxy and its environment are moving toward the south or southeast (see § 4.1.3). Note that if we do not multiply by 0.5 before the subtraction, the SW structure becomes unclear because the SW structure is a “local” excess, while on the average, the region to the north of the cD is brighter than the south in the innermost region around the cD.

Unlike the other merging galaxy clusters Abell 2142 (Markevitch et al. 2000), Abell 3667 (Vikhlinin et al. 2001b), RX J1720.1+2638 (Mazzotta et al. 2001), Abell 2256 (Sun et al. 2002), MS 1455.0+2232 (Mazzotta et al. 2002c), and 1E0657–56 (Markevitch et al. 2002), Abell 133 does not have clear surface brightness discontinuities except around the NW tongue and the complex structure within $\sim 20''$ from the center (Figures 1 and 4).

2.2. Radial Profiles of X-ray Surface Brightness and Density

In order to study the X-ray structure quantitatively, we extracted surface brightness profiles for the 0.3 – 10 keV band for three sectors shown in Figure 2. The resulting surface brightness profiles are shown in Figure 6. They were derived by accumulating counts in circular annular wedges. The range of radii covered by each annulus is shown by the horizontal bars attached to each point. There are vertical error bars, but they are too small to be easily seen in the Figure. Because of the complexity of the structure in the central regions, it is difficult to select a center for the sectors. The center that we selected ($01^{\text{h}}02^{\text{m}}42^{\text{s}}.1; -21^{\circ}52'54''$, J2000) is the centroid of the bright core of the X-ray emission, which we took to be outlined by the contour having a surface brightness of 4 counts/pixel (0.3–10 keV). As is obvious from Figure 2, the sector center does not coincide with the position of the cD galaxy ($01^{\text{h}}02^{\text{m}}41^{\text{s}}.7; -21^{\circ}52'56''$, J2000), nor does it lie on any of the brighter knots of X-ray emission within the core. However, it does lie along the extension of the X-ray tongue into the center of the core, which makes it easier to isolate the surface brightness profile of the tongue (NW2 sector). With this center, the NW1 profile passes through much of the radio-emitting area outside of the region of the tongue. Also, the drop in the surface brightness associated with the edge of the bright core region (Figures 1, 4, and 5) can be studied with this center.

The SE profile shows that there is a small jump corresponding to a possible bow-shaped feature about $30''$ from the central cD (Figures 1, 4, 5, and 6). While the SE profile is relatively smooth, the NW1 profile shows a depression at $r \sim 25''$ relative to a smooth interpolation of the declining surface brightness from smaller to larger radii. The position

of this depression corresponds to that of the radio relic (Figure 2). The NW1 sector also features a high surface brightness region associated with one of the X-ray knots near the center of the cD (at $8''$). The NW2 profile shows a hump or plateau at about the same radius of the depression, followed by a very rapid drop in surface brightness at about $40''$ (Figure 6). The hump represents the tip of the X-ray tongue.

For the SE sector, we also determined the electron density profile by deprojecting the surface brightness profiles in Figure 6 assuming that the density distributions are spherically symmetric and the density is constant in spherical shells (Figure 7). In the SE sector, the density declines smoothly except for a small jump at a radius of about $30''$, which corresponds to the small jump in Figure 6. For the NW sectors, we show the density profiles outside the tongue and the relic because the assumption of spherical symmetry is not correct in the central regions.

3. Spectral Analysis

Although we analyze the spectra in detail for a number of regions, a sense of the overall temperature distribution of the cluster can be found from an X-ray color image. For three energy bands ($0.3 - 1.5$, $1.5 - 2.5$, and $2.5 - 10$ keV), we make adaptively smoothed images as in Figure 1b. We allocate the colors of red, green, and blue to the $0.3 - 1.5$, $1.5 - 2.5$, and $2.5 - 10$ keV band images, respectively, and combine the three images. Figure 8 shows the result; the cluster center and the tongue are red, implying that these contain cooler gas. In particular, the tip of the tongue appears to be the coolest. There are no strong, sharp features which are blue (hard spectra due to hot gas) and which might be attributed to shocks.

We extracted spectra in the $0.7 - 10$ keV band in PI channels from selected regions of the *Chandra* image using the CIAO⁹ software package. We used the gain file `acisD2000-01-29gainN0001.fits` and the fef file `acisD2000-01-29fef-piN0001.fits`. Both the response matrix files and the ancillary response files were calculated using the CALCRMF/CALCARF¹¹ 1.07 package written by Alexey Vikhlinin and Jonathan McDowell. The package weighted the response files by the X-ray brightness over the corresponding image region. The spectra were grouped to have a minimum of 20 counts per bin, and fitted with one or two thermal models (MEKAL, Kaastra 1993; Liedahl, Osterheld, & Goldstein 1995) using XSPEC 11.00. In general, we allowed the absorbing column to vary from the Galactic value. In some regions, we fitted the spectra with a power-law model. Errors on fitted spectral parameters are given

¹¹See <http://asc.harvard.edu/cont-soft/software/>.

at the 90% confidence level.

3.1. Average Spectrum

First, we studied the average spectrum extracted from the innermost circular region of 2.5 radius. We found that this spectrum cannot be reproduced by a single thermal component (Table 1), because this cluster has a temperature gradient (§ 3.2). The temperature at the cluster center is much lower than that in the outer region, so we fitted the spectrum with two thermal components with the same absorption. We assumed that the metallicities of the two thermal components were the same, because we could not constrain the metal abundance when they were fitted independently. We show the result in Table 1. For comparison, we present the previous results on Abell 133 from the *Einstein* and *EXOSAT* observatories (David et al. 1993; Edge & Stewart 1991). The higher of the two temperatures obtained with *Chandra* is consistent with the temperatures obtained from *Einstein* and *EXOSAT*. Because of their relatively large fields, *Einstein* and *EXOSAT* appear to be affected by the temperature of the outer region. The *Chandra* flux is smaller than that measured previously because our spectrum applies only to the central portion of the cluster. The *Chandra* hydrogen column density is higher than the Galactic value ($1.58 \times 10^{20} \text{ cm}^{-2}$; Stark et al. 1992).

3.2. Radial Gradients in the Spectra

Figure 9 shows the radial profiles of temperature for four sectors. The position angles are $0^\circ - 90^\circ$ (NE), $90^\circ - 180^\circ$ (SE), $180^\circ - 270^\circ$ (SW), and $270^\circ - 360^\circ$ (NW), where the angles are measured from north through the east. The center of the sectors is the same as that of the sectors in Figure 2. For the NW sector, we derive the temperature of the X-ray tongue separately from that of the surrounding emission. The spectra were fitted by a MEKAL model with variable absorption. For most regions, the single temperature model can reproduce the spectra ($\chi^2/\text{dof} \lesssim 1.3$), where dof is the degrees of freedom, except for the region of the tongue ($\chi^2/\text{dof} = 1.58$). In Figure 9, the temperature increases gradually outward except for the NW sector. For the NW sector, the temperature shows a sudden rise with radius at $r \sim 20''$ for the profile excluding the tongue. A radius of $r \sim 20''$ corresponds to the southern edge of the deficit of X-ray emission associated with the radio relic (Figure 6). The fitted absorbing column density in the central regions is $N_{\text{H}} \lesssim 1 \times 10^{21} \text{ cm}^{-2}$. The profile is not inconsistent with a uniform absorbing column. The temperature profiles in Figure 9 do not change significantly even if we fix the absorbing column density at the Galactic value

($1.58 \times 10^{20} \text{ cm}^{-2}$; Stark et al. 1992).

3.3. Spectra for X-ray Tongue and Radio Relic

We investigated more closely the X-ray spectra of the regions containing the radio relic and the tongue. The regions are shown in Figure 10. In the radio relic, our main purpose was to detect or limit the contribution of nonthermal inverse Compton (IC) emission to the spectrum. We first fitted each region’s spectrum using a single temperature model with a variable absorbing column density N_{H} . This model is referred to as “1T”. The free parameters in this model are the temperature, T , the metallicity of the gas, Z , measured relative to the solar photosphere values of Anders & Grevesse (1989), the absorbing column density, N_{H} , and the normalization, K . In the “1TPL” model, we added a power-law component to the 1T model. Thus, the normalization and the power-law photon index (Γ) were added to the free parameters. On the other hand, we fixed the metallicity in the 1TPL model at the value of the 1T model, because it could not be constrained. Given the radial temperature gradient (Figure 9), spectral complexity may also result from several different emission temperatures along the line of sight. Thus, we also tried a two-temperature model “2T” with a variable absorption. We assume that metallicities of the two thermal components are the same.

For the radio relic region, the model with a power-law nonthermal component (1TPL) is slightly favored (Table 2 and Figure 11a). However, the difference in χ^2 is not very significant. Given the likely calibration uncertainties, we do not regard the detection of a power-law component as established. Instead, we take the upper limit on the flux of this component as an upper limit on any power-law nonthermal spectral component. The upper limit on the 0.3 – 10 keV flux of the power-law component is $7.1 \times 10^{-13} \text{ erg cm}^{-2} \text{ s}^{-1}$. We discuss the implications of this in §4.2.2.

The spectrum of the X-ray tongue is not fitted very well by a single temperature model, but is fitted adequately by either the 2T or 1TPL model. The 2T model is a somewhat better fit. In the 1TPL model, the fraction of the flux in the power-law component is relatively small (24% of the 0.3–10 keV flux), so most of the emission is thermal and relatively cool in any case. We note that the emission from the tongue can be explained by the superposition in projection of cold thermal emission from the small volume of the tongue, and the ambient hotter thermal emission in the cluster in front of and behind the tongue. This would account naturally for the need for two temperature components. To test this idea, we tried a model in which we fixed the absorbing column, the temperature, and the metallicity of the hotter gas spectral component to those derived from the spectrum of the region surrounding the tongue. We also fix the normalization of the hotter component to the expected value given

the foreground and background volume of the tongue region. This model is listed as “2T” in Table 2. The f-test indicates that this constrained model is as good a fit as the unconstrained two temperature model. We find that the intrinsic temperature of the cold gas in the tongue is 1.3 keV in the 2T’ model. In this model, the metallicity of the cooler component in the tongue is allowed to differ from that of the surrounding gas; the best-fit value is slightly lower but agrees within the errors. Nonthermal emission from the tongue is not required (Table 2 and Figure 11b). In this projection model, we assume that the tip of the tongue is a sphere with a radius of 8 kpc = 7.5”. The required electron density in the tongue is approximately 0.03 cm^{-3} , which implies that the tongue is nearly in pressure equilibrium with the ambient medium at the same radius, whose pressure is $0.026 \text{ keV cm}^{-3} = 4.2 \times 10^{-11} \text{ dyn cm}^{-2}$.

While there is a peak in the X-ray surface brightness at a position that nearly coincides with the center of the cD galaxy which is the host of a radio source, it is uncertain whether this is a peak in the density of the diffuse X-ray gas or X-ray emission from an AGN. We determined the X-ray spectrum from a circular region with a radius of 5” centered on the X-ray brightness peak. The emission appears to be purely thermal, and does not show any evidence for a nonthermal, power-law component. The spectrum was consistent with an absorbing column that is identical to that for the surrounding region. These both suggest that the peak is emission from diffuse hot gas, and not primarily due to an AGN.

3.4. Cooling Flow Spectrum

In the central regions of the Abell 133 cluster, the gas densities are high and the radiative cooling times are short. Thus, we fitted the spectra of the inner regions using a cooling flow model. For ease of comparison with Figure 9, the spectra were accumulated in a number of annuli, centered on the center of the sectors in Figure 2. The radii of the three annuli were selected to cover the central bright region except the tongue, the region containing the tongue, and the largest outside region fitting completely on the S3 chip. As a spectral model, we use the MKCFLOW model based on the MEKAL plasma emission code. We include any intrinsic absorption, ΔN_{H} , that may be acting on the cooling flow in the core of the cluster using the ZWABS model. Moreover, we add a MEKAL model representing the emission of the ICM outside the cooling flow, subject to Galactic absorption using the WABS model. We fix the Galactic absorption at $1.58 \times 10^{20} \text{ cm}^{-2}$ (Stark et al. 1992). The combination of the models is similar to that of Schmidt, Allen, & Fabian (2001):

$$\begin{aligned} \text{Model}_{\text{cf}} = & \text{WABS}_{\text{Gal}} \times [\text{MEKAL}(T_{\text{High}}; Z; K) \\ & + \text{ZWABS}(\Delta N_{\text{H}}) \times \text{MKCFLOW}(\dot{M})]. \end{aligned} \quad (1)$$

The free parameters are given in parentheses. The intrinsic absorption ΔN_{H} acts only on the cooling flow emission. The normalization of the MKCFLOW model, \dot{M} , is the so-called cooling rate or mass deposition rate of the flow. We fix the metallicity Z and initial gas temperature T_{High} in the MKCFLOW component to the values of metallicity and temperature of the MEKAL component, respectively. The results are shown in Table 3. The total mass deposition rate, $\dot{M}(< r)$, increases outward. We note that the mass deposition rate of the whole region ($86_{-24}^{+26} M_{\odot} \text{ yr}^{-1}$; $r < 161$ kpc) is somewhat larger than the deposition rate of $56_{-34}^{+36} M_{\odot} \text{ yr}^{-1}$ (corrected to $H_0 = 70 \text{ km s}^{-1} \text{ Mpc}^{-1}$) from White et al. (1997), although the errors overlap. For the entire region, the luminosity of the cooling flow component is $2.5 \times 10^{43} \text{ erg s}^{-1}$.

We note that if we do not use the data below 0.9 keV, ΔN_{H} is significantly reduced (parenthesis in Table 3), and at the same time, \dot{M} also decreases. Both ΔN_{H} and \dot{M} strongly depend on the data below 0.9 keV and they correlate with one another. This effect suggests that there may still be some calibration uncertainties for *Chandra* below 0.9 keV. Thus, we regard the evidence for excess absorption as preliminary.

4. Discussion

4.1. The Origin of the X-ray Tongue

The most prominent feature of the *Chandra* image of Abell 133 is the tongue of colder X-ray emitting gas that extends from the center. Cold filaments similar to the tongue are seen in A1795 and MKW3s with *Chandra* (Fabian et al. 2001; Mazzotta et al. 2002a) and in Virgo with *XMM-Newton* (Belsole et al. 2001) and *ROSAT* (Böhringer et al. 1995). We discuss several possible explanations for the tongue. The four panels in Figure 12 illustrate these possibilities schematically.

4.1.1. A Cooling Wake

One possible origin of the tongue is a cooling wake (Figure 12a). That is, the tongue might be gas which is cooling from the hot ICM, attracted into a wake along the path of the moving cD galaxy (David et al. 1994; Fabian et al. 2001). However, the temperature discontinuity between the tongue and the ambient hot gas is very sharp. We extracted the X-ray spectra of $5''$ wide regions along but just outside both sides of the tongue and find the temperature is $2.7_{-0.5}^{+0.5} \text{ keV}$, which is significantly higher than that of the tongue ($1.7_{-0.1}^{+0.0} \text{ keV}$). This shows that the temperature of the gas changes on a scale of $\lesssim 5$ kpc. If the cooling

wake scenario is correct, we expect a smooth temperature profile around the tongue. Thus, our result does not seem to support the idea that the tongue is the cooling gas accreted from the ambient hot gas.

4.1.2. Convection by a Cluster Merger

Recently, numerical simulations of cluster mergers by Ricker & Sarazin (2001) showed that ram pressure induced by a cluster merger can displace the core gas from the cluster’s potential center. As a result, the gas becomes convectively unstable, and in some cases, a convective plume of low entropy gas is formed. In the region of this plume, the variations in entropy of the gas are much greater than the variations in the pressure; thus, the low entropy plume has a high density, a low temperature, and a very high X-ray emissivity. The plume and wings with low entropy gas shown at $t = 5.75$ and 6.00 Gyr in Figure 14 of Ricker & Sarazin (2001) are remarkably similar to the X-ray distribution of Abell 133 (Figures 1 and 5). Thus, based on the X-ray image alone, merger-induced convection would be a strong candidate to explain the origin of the X-ray tongue and overall X-ray morphology of the core of Abell 133.

However, other observations are not fully consistent with this scenario, at least if the simulations in Ricker & Sarazin (2001) are typical. In this mechanism, the plume of dense gas must be falling towards the center of the cluster potential, and Figure 14 in Ricker & Sarazin (2001) shows that the tip of the plume should be at the center of the cluster potential. Since the stars in the cD galaxy will not be displaced by ram pressure, the optical center of the cD galaxy should be near to the center of the cluster potential. However, the *Chandra* image shows that the cD galaxy is not at the tip of the X-ray tongue (Figure 2). It is possible that the cD galaxy has orbital motion which results in a separation from the center of the cluster potential. In support of this idea is the observation that the cD is displaced from the center of the cluster determined on larger scales from the X-ray image (§ 2.2).

The time when the convective plume is seen corresponds to the time between the ($b = 2r_s$), +2 Gyr and +3.5 Gyr panels in Figures 6 and 7 of Ricker & Sarazin (2001). At this time, a smaller merging subcluster should be located ~ 0.5 Mpc to the northwest of the main cluster center. Merger shocks would be located to the southeast (~ 1 Mpc) and to the northwest near the smaller subcluster. There is no clear optical evidence for a concentration of galaxies or a cD galaxy to the northwest where the subcluster should be located. Moreover, an X-ray image obtained with *ROSAT*, which has a larger field of view than *Chandra*, showed that there is no significant substructure at larger radii (Rizza et al. 2000).

If this merger scenario can be applied to Abell 133, the radio relic may be induced by a shock associated with the same merger. This would probably require that the merger be at a slightly later stage than suggested by the Ricker & Sarazin (2001) simulations, and that the smaller subcluster (located to the northwest) is now falling back into the main cluster (just after the $[b = 2r_s]$, +3.5 Gyr panels in Figures 6 and 7 of Ricker & Sarazin 2001). A weak bow shock would be formed ahead of this subcluster; this shock would now be located between the subcluster and the cD galaxy of Abell 133, and might be accelerating particles to form the observed radio relic. It would be a coincidence that the tip of the X-ray tongue and the radio relic overlapped. Moreover, we do not find a temperature jump corresponding to a shock at the position of the radio relic. Below, we argue more generally that the radio relic is not produced by a merger shock (§ 4.2.1).

4.1.3. Kelvin-Helmholtz Instability

The complicated X-ray structures in the inner region of the cluster ($r \lesssim 20''$) and in the tongue suggest that some instability is developing at the cluster center. In this subsection, we show that the Kelvin-Helmholtz (KH) instability is a possible candidate. In fact, the shift of the cD galaxy from the X-ray geometrical center to the SE and the bird-like feature in Figure 5 may suggest that the galaxy is moving toward the SE.

In contrast with Abell 133, distinct smooth discontinuities of surface brightness or cold fronts have been found for Abell 2142, Abell 3667, RX J1720.1+2638, A2256, and MS 1455.0+2232 (Markevitch et al. 2000; Vikhlinin et al. 2001b; Mazzotta et al. 2001; Sun et al. 2002; Mazzotta et al. 2002c). For these clusters, the cold front is interpreted as the boundary between cold gas around the central cD galaxies and the ambient hot gas. From the shape of the cold front, the authors concluded that the cD and any associated subcluster are moving in the direction of the cold front. Vikhlinin et al. (2001a) indicated that the KH instabilities on small scales must be suppressed over an extended region (angular width $\sim 30^\circ$) near the stagnation point at the cold front for Abell 3667, and that magnetic fields are likely to be responsible for this suppression. On larger scales, the relatively smooth distributions of the cold gas at the forward edge of these cold fronts suggest that the KH instability on the scale of the entire cold core is also suppressed or has not developed to the level that it significantly changes the core shape for these clusters.

When a gravitational field exists, perturbations at a sharp interface with wavenumber less than k are stable if

$$g \gtrsim \frac{\rho_1 \rho_2 k U^2}{\rho_2^2 - \rho_1^2} = \frac{D k U^2}{D^2 - 1}, \quad (2)$$

where g is the gravitational acceleration at the interface between a high density region with density ρ_2 which is moving with a relative velocity U through a surrounding medium with a lower density ρ_1 (Paterson 1983), and the density contrast is $D \equiv \rho_2/\rho_1$. If the high density gas is approximately isothermal and hydrostatic in the gravitational field of the cD galaxy and/or an associated subcluster, and the gravitational field is approximated by an isothermal sphere, then the gravitational acceleration is roughly

$$g \approx \frac{2k_B T_2}{\mu m_H r_2}, \quad (3)$$

where k_B is the Boltzmann constant, T_2 is the temperature of the high density region, μ is the mean molecular weight (0.61), m_H is the hydrogen mass, and r_2 is the radius of the high density region. We note that equation (3) may somewhat overestimate the gravitational acceleration. This can occur if the outer part of a subcluster is stripped by tidal forces, and only the core with a flat density distribution remains. On the other hand, if the center of the subcluster has a density cusp rather than a core, equation (3) will give a more accurate estimate (e.g. Fig. 6 in Klypin et al. 1999).

We are interested in the largest scale KH instabilities with $k \sim k_0 \equiv 2\pi/r_2$ which would lead to a significant disruption of the entire cold front. Then, equations (2) and (3) can be rewritten to show that the gas will be stable if

$$U \lesssim U_{\text{KH}} \equiv \sqrt{\frac{k_B T_2}{\pi \mu m_H} \frac{D^2 - 1}{D}}. \quad (4)$$

On the other hand, if gravity is unimportant, the growth rate in the linear regime at a flat interface between two incompressible fluids with different densities and relative motion is given by

$$\omega = k \frac{D^{1/2} U}{1 + D}, \quad (5)$$

(Drazin & Reid 1981). Here, we set $k \sim k_0 = 2\pi/r_2$. Murray et al. (1993) showed that conditions (4) and (5) are consistent with results of numerical simulations.

In Table 4, we compare the values of U_{KH} and $t_{\text{KH}} = 2\pi/\omega$ for the cold fronts in Abell 133, Abell 2142, Abell 3667, RX J1720.1+2638, MS 1455.0+2232 and 1E0657–56. The observed parameters T_2 , r_2 , and D used to derive the KH instability parameters were taken from Markevitch et al. (2000), Vikhlinin et al. (2001b), and Mazzotta et al. (2001, 2002c) and Markevitch et al. (2002). Because Sun et al. (2002) do not give the density contrast D for Abell 2256 due to the complicated geometry of the substructure, we do not discuss its cold front in the following. We assume that the cD galaxy of Abell 133 is moving toward the SE. However, there is no clear large density jump in that direction (Figure 7),

and we assume that the density jump was disrupted by the KH instability. As an upper limit, we assume the density jump prior to disruption is less than the change in density from $r \approx 10''$ to $30''$, which is the region over which the temperature rises rapidly. However, there is a small jump in the density $D \approx 1.3$ at a radius of $r \approx 30''$ (Figure 7). If we instead adopt this value of D , then the maximum velocity to avoid disruption by the KH instability is reduced to $U_{\text{KH}} \sim 200 \text{ km s}^{-1}$. For Abell 2142, Abell 3667, and RX J1720.1+2638, we also present the velocities of the cold cores, U_{obs} , obtained from the stagnation condition at the cold front (Markevitch et al. 2000; Vikhlinin et al. 2001b; Mazzotta et al. 2001). We used U_{obs} to derive t_{KH} . For Abell 133, we derived t_{KH} by assuming that the core velocity is larger than the upper limit on U_{KH} . For MS 1455.0+2232, Mazzotta et al. (2002c) do not present U_{obs} because of large temperature uncertainties. Thus, we derived t_{KH} by assuming $U < U_{\text{KH}}$.

The small value of U_{KH} for Abell 133 shows that the cold core is more vulnerable to the KH instability than in Abell 2142, Abell 3667, RX J1720.1+2638, and MS 1455.0+2232. This may show that there is more variety in the depths of the potentials of substructures around cD galaxies than might be expected from the similarity in their optical properties. Note that Table 4 suggests that gravity cannot completely suppress the KH instability on large scales even for Abell 2142 and Abell 3667 ($U_{\text{obs}} > U_{\text{KH}}$). Magnetic fields may have aided in the suppression of large scale as well as small scale instabilities in these cases (see Vikhlinin et al. 2001a). Alternatively, if the cores started to move very recently, the KH instability may have just started to develop (Mazzotta, Fusco-Femiano, & Vikhlinin 2002b), and the cores might not have been disrupted yet. In Table 4, we also present the values for 1E0657–56, which was recently observed by Markevitch et al. (2002). For this cluster, t_{KH} is extremely low because of the high velocity, U_{obs} . In fact, most of the cold gas around the substructure appears to be removed (Markevitch et al. 2002). Abell 133 seems to be intermediate between 1E0657–56 and the other four clusters in the level of KH instability and in the size of the cold front.

To assess the degree of KH instability more quantitatively, we calculate the ratio $t_{\text{cross}}/t_{\text{KH}}$, where t_{cross} is the crossing time of the cool core in the cluster (Mazzotta et al. 2002b). The larger $t_{\text{cross}}/t_{\text{KH}}$ is, the more vulnerable the core is to the KH instability. We estimate the crossing time t_{cross} from the core velocity and the maximum cluster radius that a core can reach, r_{max} . Let the current radius of the core be r , and let r_{200} be the cluster radius within which the average mass density is 200 times the critical density of the Universe (ρ_{cr}):

$$r_{200} \equiv \left(\frac{3M_{200}}{800\pi\rho_{\text{cr}}} \right)^{1/3}, \quad (6)$$

where M_{200} is the mass of the cluster within r_{200} . For this estimate of t_{cross} , we will assume

that the core has a radial orbit. Then, the maximum radius r_{\max} of the core is given by

$$(1/2)U_{\text{obs}}^2 = \Phi(r_{\max}) - \Phi(r) , \quad (7)$$

where $\Phi(r)$ is the cluster gravitational potential at r . If a cluster has an isothermal density distribution (density $\propto r^{-2}$), the potential difference is given by

$$\Phi(r_{\max}) - \Phi(r) = \frac{GM_{200}}{r_{200}} \ln \frac{r_{\max}}{r} . \quad (8)$$

From equations (7) and (8), we obtain

$$r_{\max} = r \exp \left(\frac{r_{200}U_{\text{obs}}^2}{2GM_{200}} \right) . \quad (9)$$

The cluster mass M_{200} can be derived from cluster temperature T_1 using an empirical relation. Reiprich (2001) found the relation of

$$\log \left(\frac{1.4M_{200}}{M_{\odot}} \right) = 13.735 + 1.710 \log \left(\frac{T_1}{\text{keV}} \right) \quad (10)$$

from the X-ray data of 88 clusters. The observed cool cores appear to be near the cluster centers. Of course, we do not know where in the orbit the core started, or how many times it has passed near the cluster center. Thus, we crudely estimate the crossing times as $t_{\text{cross}} = r_{\max}/U_{\text{obs}}$.

In Table 4, we present the values of T_1 , r_{\max} , t_{cross} , and $t_{\text{cross}}/t_{\text{KH}}$. We assume $r = 0.2r_{200}$ for all the clusters. For Abell 133, we assume that U_{obs} is larger than the upper limit on U_{KH} , while for MS 1455.0+2232 we assume that $U_{\text{obs}} < U_{\text{KH}}$. Table 4 shows that the value of $t_{\text{cross}}/t_{\text{KH}}$ for Abell 133 is intermediate between that for 1E0657–56 and those for the other four clusters. This supports our argument about the relative level of KH instability in these clusters.

Ram pressure from the ambient gas is also expected to affect the cold gas around a cD galaxy. Sarazin (2001) indicated that ram pressure would affect the cold gas distribution at a radius which satisfies

$$P_{\text{ram}} \gtrsim P_{\text{cool}}(r) , \quad (11)$$

where P_{cool} is the static pressure of the gas around the cD galaxy. Since the cD galaxy is not at the geometrical center of Abell 133 (Figure 2), we expect that the relation is satisfied even at $r \sim 0$. Figures 7 and 9 show that the pressure in the central region of the cluster is $P_{\text{cool}}(0) \sim 1.1 \times 10^{-11}$ dyn cm $^{-2}$. Since there is no clear cold front for this cluster, we take the gas density around the cluster center, $n_e = 0.05$ cm $^{-3}$, as the density of the gas

streaming relative to the cD galaxy (Figure 7). In this case, the relative velocity of the cD galaxy to the surrounding gas must be larger than about 400 km s^{-1} to satisfy the relation (11) at $r \sim 0$. This velocity is very similar to U_{KH} . We note that the criteria for those two mechanisms, the KH instability and ram pressure, should be similar because both involve the competition between the momentum in the flow and gravitational acceleration.

Since the X-ray substructure around the cD galaxy of Abell 133 is fragile as is shown by the large $t_{\text{cross}}/t_{\text{KH}}$, it is unlikely that it is a merged subcluster that has survived a violent merger. As proposed for RX J1720+2638 and MS 1455.0+2232, an alternative scenario which may explain the presence of the moving substructure is that it may be the result of the collapse of two different perturbations in the primordial density field on two different linear scales at nearly the same location in space (Mazzotta et al. 2001, 2002c). As the density perturbations grew, the smaller scale perturbation collapsed first and formed the substructure around the cD galaxy. The larger scale perturbation collapsed more recently, and forms the main body of Abell 133. The substructure around the cD galaxy was initially located slightly offset from the center of the cluster and it is now oscillating around the minimum of the cluster potential well. Since the initial position of the substructure is near to the cluster center, it is likely that the velocity is subsonic. Recently, Fujita et al. (2002) showed quantitatively that substructures tend to be located near the cluster centers.

Mazzotta et al. (2001) estimated the formation redshift of the central subclump in RX J1720+2638 using a relation between the formation redshift and the temperature of a cluster. However, Fujita & Takahara (1999) showed that this relation has a large dispersion, because for a given spatial scale the amplitude of initial perturbations can vary significantly. Even with this caveat, the low temperature of the gas around the cD galaxy of Abell 133 (1.4 keV) suggests a large formation redshift for the substructure ($z \gtrsim 1$) if the virial radius was smaller than 0.5 Mpc (Figure 5b in Fujita & Takahara 2000).

Since the cD galaxy is located to the SE of the radio relic and it seems to be moving to the SE, it might be responsible for the relic. Slee et al. (2001) estimated that the age of the relic is $t_{\text{radio}} = 4.9 \times 10^7 \text{ yr}$. If the cD galaxy were located at the position of the relic when the relic was formed, the velocity of the galaxy must be $\gtrsim 700 \text{ km s}^{-1}$ in the plane of the sky. This velocity is larger than U_{KH} (Table 4). On the other hand, the relative velocity between the cD galaxy and the whole cluster is 220 km s^{-1} along the line of sight (Way et al. 1997). This would require that the cD velocity be at an angle of $< 17^\circ$ with respect to the plane of the sky. The value of t_{radio} may be somewhat larger than $4.9 \times 10^7 \text{ yr}$, the transverse velocity may be somewhat smaller than 700 km s^{-1} , and/or the radio source may have been formed at some distance from the center of the cD galaxy, as is generally true of radio lobes. On the other hand, if the radio relic itself is moving to the NW with the velocity

of $\sim 500 - 600 \text{ km s}^{-1}$ (Mach number $0.6 - 0.7$) as a result of buoyancy (§ 4.1.4), the KH model may be more easily reconciled with the radio relic age.

4.1.4. Uplifted Gas by a Buoyant Bubble

Recent *Chandra* X-ray observations (e.g., Fabian et al. 2000; McNamara et al. 2000; Blanton et al. 2001; Mazzotta et al. 2002a) and earlier *ROSAT* images (e.g., Böhringer et al. 1993) show that radio sources at the centers of several clusters are inflating bubbles in the ICM, which presumably consist of relativistic particles, magnetic fields, and possibly extremely hot thermal gas of low density. The radio bubbles have low X-ray surface brightnesses, presumably since the radio plasma has displaced the ICM. These hot bubbles are buoyant and should be moving outward in the cluster gravitational potential. Recent numerical simulations show that these hot bubbles may uplift cooler gas from the cluster center (Churazov et al. 2001; Quilis, Bower, & Balogh 2001; Brüggén & Kaiser 2001). The nonthermal plasma in the bubble can produce radio emission, while the uplifted dense, cool thermal gas will emit strongly in the X-ray band. The predicted configuration of a radio emitting bubble and uplifted X-ray gas is very similar to the one observed for Abell 133 (Figure 2) and also in the Virgo cluster (Churazov et al. 2001). Thus, the X-ray and radio observations may suggest that a bubble including the radio relic is uplifting the cold tongue from the cluster center. The deficit in X-ray surface brightness at the radio relic can also be explained by this picture (Figure 6). Moreover, the fact that the tongue seems to be in pressure equilibrium with the ambient medium is also favorable to this model (Churazov et al. 2001; Brüggén & Kaiser 2001). However, assuming the tongue results from the buoyant motion of the bubble, there should be another umbrella-like X-ray excess emission at the head of the bubble due to compression of cool gas ahead of the bubble, if the buoyant motion is in the plane of the sky (see the upper right figure of Figure 8 in Churazov et al. 2001). Since the emission is not observed, the tongue and the bubble may not be in the plane of the sky as is shown in the bottom right figure of Figure 8 in Churazov et al. (2001). For example, if the buoyant motion were at an angle 45° with respect to the plane of the sky and the bubble’s depth along the line of sight is the same as its width ($\sim 50 \text{ kpc}$), the observed decrease in surface brightness ($\sim 30 \%$; Figure 6) would be consistent with the idea that the bubble is deficient in X-ray-emitting gas.

If we assume the age of the relic is $t_{\text{radio}} = 4.9 \times 10^7 \text{ yr}$ (Slee et al. 2001), and the bubble including the relic was formed around the cD galaxy, the relative upward velocity must be $v_{\text{bub}} > 700 \text{ km s}^{-1}$. More realistically, if the velocity vector of the relic is at 45° to the plane of the sky and the relic was formed by jet activity away from the cD galaxy, say at a distance

of ~ 10 kpc from the cD, the upward velocity is still $v_{\text{bub}} \sim 700 \text{ km s}^{-1}$. The sound velocity of the surrounding gas ($T \sim 3 \text{ keV}$) is $\sim 900 \text{ km s}^{-1}$. Thus, the Mach number of the rising bubble is similar to the values of $\mathcal{M} \sim 0.6 - 0.7$ predicted by Churazov et al. (2001).

Assuming that the density of the tip of the tongue is 0.03 cm^{-3} and the temperature is 1.3 keV (§ 3.3), the radiative cooling time is $4 \times 10^8 \text{ yr}$. This is about an order of magnitude longer than the estimated age of the radio relic. Thus, if the tongue was uplifted by the buoyant motion of the radio relic, the low temperature of the tongue cannot be the result of radiative cooling at its current position. The gas in the tongue presumably cooled radiatively when the gas was located closer to the center of the cD before it was uplifted. In addition, adiabatic cooling may have lowered the temperature further as the gas was lifted to regions with a lower ambient gas pressure.

Given the high density of gas in the tongue and its large volume, one concern is whether the radio bubble could lift such a large mass and remain buoyant. For the purpose of this estimate, let us assume that the radio relic is filled with nonthermal and possibly thermal plasma having a very low density so that its X-ray emissivity is low. detection. We further assume that the extent of the radio bubble along the line of sight is similar to its largest diameter in the plane of the sky; we treat the radio bubble as an oblate spheroid. This is consistent with the flattened, “mushroom cloud” shape expected for a buoyant bubble (Churazov et al. 2001). Then, the total volume of the radio bubble is $V_{\text{bub}} \approx 4.3 \times 10^4 \text{ kpc}^3$. On the other hand, we assume that the extent of the tongue along the line of sight is similar to its narrower dimension; we treat it as a prolate spheroid, which is consistent with the uplifted trail below a convective bubble (Churazov et al. 2001). Then, the volume of the tongue is $V_{\text{ton}} \approx 1.8 \times 10^3 \text{ kpc}^3$. For an average tongue density of 0.03 cm^{-3} , this implies a total mass of $M_{\text{ton}} \sim 2 \times 10^9 M_{\odot}$. Thus, the average density of the material in the radio bubble and tongue combined is $\sim 0.001 \text{ cm}^{-3}$. This is still much lower than the typical gas densities at similar distances on either side of the cD galaxy in Abell 133 (Figure 7). Thus, it is at least plausible that the radio bubble could have lifted the tongue via buoyancy.

It is interesting to estimate the impact of the radio bubble on the cooling flow of Abell 133. If bubbles transport a large amount of cold gas from the cluster centers to the periphery of cooling flows, they may explain the lack of cooled gas in the cooling flows (Peterson et al. 2001; Kaastra et al. 2001; Tamura et al. 2001). As noted above, the total mass of the tongue is $M_{\text{ton}} \sim 2 \times 10^9 M_{\odot}$. This material has been lifted over the lifetime of the radio relic, which implies an average outflow rate of $\dot{M}_{\text{ton}} \sim 40 M_{\odot} \text{ yr}^{-1}$. This is somewhat smaller than the cooling inflow rate derived from the X-ray spectrum on the same radial scale (Table 3). However, the total cooling radius for Abell 133 is much larger than the size of the X-ray tongue (White et al. 1997). Thus, the tongue seems to reside well within

the cooling radius of the cluster, and would therefore not actually transport gas outside of the cooling radius. Moreover, as is shown in Table 3, the mass deposition rate derived by spectral analysis is increasing outward at the position of the tongue. So, buoyant mass transport may affect the local mass cooling inflow rate near the center of Abell 133, but it probably does not affect the overall cooling rate.

The energy associated with the expansion and motion of the radio bubble might affect the energetics of the X-ray gas, and might partially counteract radiative cooling (Böhringer et al. 2002). Assuming that the radio bubble is adiabatic, the work done by the radio bubble on the surrounding gas is

$$W_{\text{bub}} = \int_{V_0}^{V_1} P dV = \int_{V_0}^{V_1} P_0 V_0^\gamma \frac{dV}{V^\gamma} = \frac{P_0 V_0 - P_1 V_1}{\gamma - 1}, \quad (12)$$

where P and V are the pressure and the volume of the radio bubble, respectively, and γ is the adiabatic constant. The subscripts 0 and 1 stand for the values when the radio bubble is formed and those at present, respectively. If we assume that the radio bubble was formed near the cluster center and has been nearly in pressure equilibrium with the surrounding gas, $P_0 = 1.7 \times 10^{-10}$ and $P_1 = 7.9 \times 10^{-11}$ dyn cm $^{-2}$ (Figures 7 and 9). Moreover, if we assume that the volume of the observed radio bubble is $V_1 = 4.3 \times 10^4$ kpc 3 and $\gamma = 5/3$, the initial volume is $V_0 = 2.7 \times 10^4$ kpc 3 and the work is $W_{\text{bub}} = 5.2 \times 10^{58}$ erg. Moreover, the gravitational energy released by matter displacement is

$$W_{\text{dis}} \approx \frac{V_1 + V_0}{2} \rho_{\text{hot}} g_{\text{ton}} l_{\text{ton}}, \quad (13)$$

where ρ_{hot} is the density of the gas surrounding the tongue, and l_{ton} is the length of the tongue. The gravitational acceleration around the tongue is given by

$$g_{\text{ton}} \approx \frac{P_0 - P_1}{\rho_{\text{hot}} l_{\text{ton}}}. \quad (14)$$

Thus, the gravitational energy is $W_{\text{dis}} \approx 9.1 \times 10^{58}$ erg, and the total energy released by the bubble motion is $W = W_{\text{bub}} + W_{\text{dis}} \approx 1.4 \times 10^{59}$ erg. If the work has been done during the past 4.9×10^7 yr, the rate of work is 9×10^{43} erg s $^{-1}$. On the other hand, the luminosity of the cooling flow component is 2.5×10^{43} erg s $^{-1}$ (see § 3.4), which is smaller than W . Thus, the energy dissipated by the expansion of the radio bubble may compensate the energy radiated by cooling gas at least for this cluster at present, although it is uncertain what fraction of the dissipated energy is converted to thermal energy (but see Quilis et al. 2001).

Although the buoyant radio bubble model may explain the observed tongue, at present it is not clear what conditions are required to produce uplifting of dense cool gas. For example, the numerical simulations of Brüggén et al. (2002) do not show the formation of a cold X-ray tongue.

4.2. The Radio Relic

4.2.1. Origin of the Radio Relic

Assuming that the unusual radio source to the north of the cluster center in Abell 133 is related to the cluster, there have been at least two suggestions as to its origin. First, the source might be a cluster radio relic (e.g., Slee et al. 2001). Radio relics are diffuse radio sources with steep spectra which are not associated with a radio galaxy in the cluster and which are generally located far from the center of the cluster (e.g., Röttgering et al. 1997). Generally speaking, radio relic sources tend to be moderately polarized. This and their outer location distinguish radio relics from radio halos. Radio relics (and radio halos) are generally associated with clusters which appear to be undergoing a merger. A common theoretical interpretation is that radio relics are produced by acceleration, re-acceleration, or adiabatic compression of relativistic electrons and magnetic fields by merger shocks.

Some of the radio properties of the source in Abell 133 seem at variance with those of other cluster radio relics. First, the radio source is projected only ≈ 40 kpc from the cD galaxy of Abell 133. Of course, it is possible that it is actually at a much larger radial distance, and only appears near the center in projection. There are several other radio relics seen in projection near cluster centers, including the sources in Abell 13 and Abell 4038 (Slee et al. 2001). Second, the integrated polarization of the radio relic source in Abell 133 is low ($\sim 2.3\%$ Slee et al. 2001), unlike most radio relics. However, the low integrated polarization is mainly the result of variations in the direction of the polarization across the source. Figure 13 shows the radio polarization at 1.465 GHz as a function of position in the radio relic source; the data comes from the same observations discussed in Slee et al. (2001). The data in Figure 13 are not corrected for Faraday rotation. In a number of comparatively large areas within the main body of the relic the polarized fraction varies between 3 and 20 percent, the larger fractions suggesting that either the Faraday rotation in these areas is not large or that it is fairly uniform. Note that even rotation measures as small as $RM \gtrsim 20$ rad m^{-2} would produce Faraday rotations of $\gtrsim 45^\circ$ at 1.4 GHz. In general, radio sources located near the centers of cluster cooling flows show very high Faraday rotations ($RM \gtrsim 800$ rad m^{-2} ; e.g., Taylor, Barton, & Ge 1994; Ge & Owen 1994). The fact that strong polarization is observed in the Abell 133 relic without correction for Faraday rotation may indicate the relic is located in front of, rather than within or behind, the cluster cool core.

If the radio relic were produced by a merger shock and the magnetic field were strongly affected by compression in the shock, one would expect the magnetic field direction (perpendicular to the electric vector) to be mainly parallel to the shock front. Indeed, we see in Figure 13 that the electric vectors closest to the concave northern edge of the relic have

the required orientation to suggest that this may be a shock front with a tangential magnetic field direction. Of course, any other mechanism which produced a compression of the northern edge of the radio source might have the same effect; if the radio source has risen buoyantly to the north, one might also expect some compression of this edge. However, this must be an uncertain interpretation until the electric vectors can be corrected for Faraday rotation.

Several other features in Figure 13 are of interest. The polarization near the bright knots at the tip of the X-ray tongue ($01^{\text{h}}00^{\text{m}}13^{\text{s}}.5$; $-22^{\circ}08'40''$, B1950) and further down the tongue to the SE is quite strong and particularly variable in direction. Perhaps this indicates that the relic lies behind the tongue, and that the emission from those regions of the relic suffers strong and variable Faraday rotation by the comparatively cool gas in the tongue.

In the two filaments of radio emission extending to the east and south-east, the polarizations are mainly perpendicular to the filaments, which implies that the magnetic field is parallel to them. The origin of these filaments may be connected to the magnetic field lines (e.g., Enßlin & Gopal-Krishna 2001; Enßlin & Brüggen 2002). The radio relic in Abell 133 is rather filamentary. Although there are several possible origins for this structure, Enßlin & Gopal-Krishna (2001) and Enßlin & Brüggen (2002) suggested that the structure results from the compression of old radio plasma by merger shocks.

On the other hand, our *Chandra* observations are largely inconsistent with a merger shock origin for the radio relic. First of all, no evidence for a shock is seen in the image (Figure 2), X-ray colors (Figure 8), or spectra (Figure 11) of the radio relic region. If the radio relic coincided with a shock, this region should be unusually bright in X-rays, due mainly to compression of the cluster gas in the shock. Actually, most of the radio relic region is unusually faint in X-rays (Figure 6). The exception is the region where the X-ray tongue overlaps the radio relic. However, the tongue is due to cool thermal gas, and is thus not a result of a merger shock.

An alternative explanation of the radio relic is that it is an old radio lobe from the central radio source associated with the cD galaxy in Abell 133 (Rizza et al. 2000). An early radio map of the source suggested a bridge of emission connecting the cD radio source with the radio relic (Rizza et al. 2000), but this does not appear in a more sensitive, higher resolution image (Slee et al. 2001). Many of the radio properties of the relic are consistent with its interpretation as an old radio lobe. Similar radio lobes associated with cD galaxies in cooling flow clusters generally have rather steep radio spectra (e.g., Ge & Owen 1994; Rizza et al. 2000). The displacement of the radio relic from the central cD might be due to buoyancy (§ 4.1.4), or to the motion of the central cD, perhaps as a result of a subcluster motion (§ 4.1.3). One difficulty is that one usually finds two radio lobes, presumably produced by

a double-sided jet. However, if the central cD is moving to the southeast, the two bubbles would be displaced in the same direction and might either overlap in projection or have merged together.

Our *Chandra* observations are probably more consistent with the interpretation of this radio source as a relic radio lobe formerly energized by the central cD, rather than a merger-shock generated cluster radio relic. Radio lobes associated with cD galaxies at the centers of cooling flow clusters produce holes in the X-ray emission (e.g., Fabian et al. 2000; McNamara et al. 2000; Blanton et al. 2001), suggesting that the radio plasma has displaced the thermal, X-ray emitting gas. In Abell 133, the radio relic region is also somewhat fainter in X-rays than the surrounding region (Figure 6). As noted in § 4.1.4, many properties of the X-ray tongue are consistent with gas which has been uplifted by a buoyant radio bubble. In fact, the overall radio and X-ray properties of the relic source in Abell 133 are similar to the eastern radio bubble (the “ear”) of M87 in the Virgo cluster (Owen, Eilek, & Kassim 2000). This mushroom-shaped radio bubble has a shape similar to the radio source in Abell 133, and also has a very steep radio spectrum. The M87 ear is filamentary, although mainly around its edge. In M87, there is a linear extension of X-ray emission due to cool, thermal gas which connects the center of the cluster with the radio bubble (Böhringer et al. 1995), similar to the tongue in Abell 133. The radio and X-ray structure of M87 have been interpreted as the result of a buoyant radio bubble (Churazov et al. 2001; Brüggén et al. 2002; Young, Wilson, & Mundell 2002). One difference between M87 and Abell 133 is that there is radio emission connecting the ear in M87 with the nucleus of the galaxy, while the radio relic in Abell 133 does not show any strong radio bridge with the central cD. This might be a result of a lower level of current AGN activity in the cD galaxy in Abell 133 compared to M87.

In summary, our X-ray observations are more consistent with the interpretation of the radio relic in Abell 133 as a displaced radio lobe from the central cD, rather than as a merger shock-induced relic.

4.2.2. *Magnetic Field in the Radio Relic*

In § 3.3, we found an (at best) marginal detection of nonthermal X-ray emission from a radio relic. We now use these spectral results to constrain the magnetic field in the radio relic, under the assumption that this nonthermal emission is due to inverse Compton (IC) scattering. In the model with a power-law component (Model 1TPL in § 3.3), the X-ray flux of the power-law component is 2.2×10^{-13} erg cm⁻² s⁻¹ for 2 – 10 keV and the photon index is $\Gamma = 1.7_{-1.1}^{+0.3}$. The radio synchrotron flux density of the relic is 137 mJy and flux density spectral index is $\alpha = 2.1 \pm 0.1$ (flux density proportional to $\nu^{-\alpha}$), both at 1.425 GHz (Slee

et al. 2001). For emission from a single power-law electron energy distribution, the IC and synchrotron emission have the same spectral index. This would require $\Gamma = \alpha + 1$, which is not consistent with our measured values. However, the IC X-ray emission in the *Chandra* band would be due to relatively low energy relativistic electrons, which would produce very low frequency radio emission. Both observations and models suggest that the radio spectrum is considerably flatter at lower frequencies (Slee et al. 2001), and thus the X-ray and radio spectral indices might be consistent. We will adopt the X-ray spectral index and compare the X-ray flux with the radio flux density of 35.5 ± 4.3 Jy at 80 MHz, the lowest frequency at which the flux density is determined accurately. This radio flux density includes the cD galaxy and another nearby radio source, but they are much weaker than the radio relic. Using the standard expressions for the IC and synchrotron emission assuming a power-law electron energy distribution (e.g., Sarazin 1986), we find that the required magnetic field in the relic is $B \approx 1.2 \mu\text{G}$. This is about one order of magnitude smaller than the magnetic field (Slee et al. 2001) derived from models for the radio spectral index ($B \approx 10 \mu\text{G}$) or minimum energy arguments applied to the radio flux ($B \approx 14 \mu\text{G}$). This might indicate that the magnetic field is filamentary and highly variable, which may also be suggested by the radio image of the the relic. However, given the marginal detection of the nonthermal X-ray emission and the disparity between the magnetic field values required by the radio and X-ray observations, we believe it is best to treat the X-ray spectral result as an upper limit of the nonthermal flux. This implies a lower limit on the radio relic magnetic field of $B \geq 1.2 \mu\text{G}$, which is consistent with the radio results but not constraining.

5. Conclusions

We have presented the results of a *Chandra* observation of the cluster of galaxies Abell 133. The X-ray image shows a tongue of emission extending from the cD galaxy to the NW; the tongue extends in the direction of and partially overlaps the radio relic. There is no optical counterpart of the tongue. The X-ray surface brightness at the position of the radio relic is smaller than the surrounding region except for the tongue, suggesting that the radio plasma has displaced the thermal gas in this region. The X-ray spectrum indicates that the emission from the tongue is thermal, and the temperature is distinctly lower than that of the ambient hot gas.

We discussed several possible origins for the tongue; two of these seem reasonably consistent with the X-ray and radio data. First, the tongue may be the result of a Kelvin-Helmholtz instability acting on the cool core surrounding the cD galaxy as the cD moves through surrounding, lower density gas. We show that the cD galaxy and the cold gas around it must be

moving with a velocity of $\gtrsim 400 \text{ km s}^{-1}$ for a large scale KH instability to develop between the cold core and the ambient hot intracluster medium. The critical velocity for the KH instability is several times smaller for Abell 133 than for other clusters which show smooth, well-defined cold fronts. The required motion of the cD galaxy is consistent with its offset position in the cluster relative to the X-ray centroid determined at large radii. This offset can be explained if the velocity of the cD galaxy is $\gtrsim 400 \text{ km s}^{-1}$. Thus the onset of a KH instability is at least plausible.

The second possibility is that the radio relic is a buoyant radio bubble, and that the tongue was uplifted by the motion of this bubble. Recent numerical simulations indicate that buoyant bubbles of nonthermal plasma produced by AGN activity can uplift cold gas from the cluster center (Churazov et al. 2001; Quilis et al. 2001; Brüggen et al. 2002). For Abell 133, we suggest that the bubble is the radio relic, and that it uplifts the X-ray tongue. The velocity of the radio bubble expected from the age of the radio relic is consistent with that predicted numerically. The energy dissipated by the moving bubble may affect the cooling flow in Abell 133.

The origin of the filamentary radio relic source in Abell 133 remains uncertain. It may be a radio source that is generated by a shock wave from merging clusters, similar to the relics which are often seen in the outer regions of clusters. In this case, the radio emitting electrons would have been accelerated, re-accelerated, and/or compressed by the cluster merger shock. Alternatively, the radio relic might be a displaced radio lobe (or lobes) from the radio source associated with the central cD galaxy in the cluster. The lack of evidence for a merger shock near the relic, the anti-correlation between the radio and X-ray emission across most of the relic, and the association of the relic with the tongue of cool, dense X-ray gas all are more consistent with the relic being a displaced radio lobe or bubble, rather than being a cluster merger-shock induced radio relic.

We are grateful to E. Blanton, S. Randall, I. Tanaka, and S. Oya for useful comments. Support for this work was provided by the National Aeronautics and Space Administration through *Chandra* Award Numbers GO1-2122X and GO1-2123X, issued by the *Chandra* X-ray Observatory Center, which is operated by the Smithsonian Astrophysical Observatory for and on behalf of NASA under contract NAS8-39073. L. R. acknowledges support from NSF grant AST-0071167 to the University of Minnesota. H. A. thanks CONACyT for financial support under grant 27602-E.

REFERENCES

- Anders, E. & Grevesse, N. 1989, *Geochim. Cosmochim. Acta*, 53, 197
- Belsole, E. et al. 2001, *A&A*, 365, L188
- Blanton, E. L., Sarazin, C. L., McNamara, B. R., & Wise, M. W. 2001, *ApJ*, 558, L15
- Böhringer, H., Voges, W., Fabian, A. C., Edge, A. C., & Neumann, D. M. 1993, *MNRAS*, 264, L25
- Böhringer, H., Nulsen, P. E. J., Braun, R., & Fabian, A. C. 1995, *MNRAS*, 274, L67
- Böhringer, H., Matsushita, K., Churazov, E., Ikebe, Y., & Chen, Y. 2002, *A&A*, 382, 804.
- Brüggen, M. & Kaiser, C. R. 2001, *MNRAS*, 325, 676
- Brüggen, M., Kaiser, C. R., Churazov, E., & Enßlin, T. A. 2002, *MNRAS*, 331, 545.
- Carilli, C. L., Perley, R. A., & Harris, D. E. 1994, *MNRAS*, 270, 173
- Churazov, E., Brüggen, M., Kaiser, C. R., Böhringer, H., & Forman, W. 2001, *ApJ*, 554, 261
- David, L. P., Slyz, A., Jones, C., Forman, W., Vrtilik, S. D., & Arnaud, K. A. 1993, *ApJ*, 412, 479
- David, L. P., Jones, C., Forman, W., & Daines, S. 1994, *ApJ*, 428, 544
- David, L. P., Nulsen, P. E. J., McNamara, B. R., Forman, W., Jones, C., Ponman, T., Robertson, B., & Wise, M. 2001, *ApJ*, 557, 546
- Drazin, P. G., & Reid, W. H. 1981, *Hydrodynamic Stability* (Cambridge: Cambridge Univ. Press), 126
- Edge, A. C. & Stewart, G. C. 1991, *MNRAS*, 252, 414
- Enßlin, T. A. & Brüggen, M. 2002, *MNRAS*, 331, 1011.
- Enßlin, T. A., & Gopal-Krishna 2001, *A&A*, 366, 26
- Fabian, A. C. 1994, *ARA&A*, 32, 277
- Fabian, A. C. et al. 2000, *MNRAS*, 318, L65

- Fabian, A. C., Sanders, J. S., Etti, S., Taylor, G. B., Allen, S. W., Crawford, C. S., Iwasawa, K., & Johnstone, R. M. 2001, *MNRAS*, 321, L33
- Fujita, Y., Sarazin, C. L., Nagashima, M., & Yano, T. 2002, *ApJ*, submitted
- Fujita, Y., & Takahara, F. 1999, *ApJ*, 519, L55
- Fujita, Y., & Takahara, F. 2000, *ApJ*, 536, 523
- Furusho, T., Yamasaki, N. Y., Ohashi, T., Shibata, R., & Ezawa, H. 2001, *ApJ*, 561, L165.
- Ge, J., & Owen, F. N. 1994, *AJ*, 108, 1523
- Henry, J. P. & Briel, U. G. 1995, *ApJ*, 443, L9
- Huang, Z., & Sarazin, C. L. 1998, *ApJ*, 496, 728
- Ikebe, Y. et al. 1997, *ApJ*, 481, 660
- Kaastra, J. S. 1993, An X-Ray Spectral Code for Optically Thin Plasmas (Internal SRON-Leiden Report, updated version 2.0)
- Kaastra, J. S., Ferrigno, C., Tamura, T., Paerels, F. B. S., Peterson, J. R., & Mittaz, J. P. D. 2001, *A&A*, 365, L99
- Klypin, A., Kravtsov, A. V., Valenzuela, O., & Prada, F. 1999, *ApJ*, 522, 82
- Liedahl, D. A., Osterheld, A. L., & Goldstein, W. H. 1995, *ApJ*, 438, L115
- Makishima, K. et al. 2001, *PASJ*, 53, 401
- Markevitch, M. et al. 2000, *ApJ*, 541, 542
- Markevitch, M., Gonzalez, A. H., David, L., Vikhlinin, A., Murray, S., Forman, W., Jones, C., & Tucker, W. 2002, *ApJ*, 567, L27
- Markevitch, M., Sarazin, C. L., & Vikhlinin, A. 1999, *ApJ*, 521, 526
- Markevitch, M. & Vikhlinin, A. 2001, *ApJ*, 563, 95
- Mazzotta, P., Markevitch, M., Vikhlinin, A., Forman, W. R., David, L. P., & VanSpeybroeck, L. 2001, *ApJ*, 555, 205
- Mazzotta, P., Kaastra, J. S., Paerels, F. B., Ferrigno, C., Colafrancesco, S., Mewe, R., & Forman, W. R. 2002a, *ApJ*, 567, L37

- Mazzotta, P., Fusco-Femiano, R., & Vikhlinin, A. 2002b, ApJ, 569, L31.
- Mazzotta, P., Markevitch, M., Forman, W. R., Jones, C., Vikhlinin, A., David, L. P., & VanSpeybroeck, L. 2002c, ApJ, submitted (astro-ph/0108476)
- McNamara, B. R. et al. 2000, ApJ, 534, L135
- Murray, S. D., White, S. D. M., Blondin, J. M., & Lin, D. N. C. 1993, apj, 407, 588
- Owen, F. N., Eilek, J. A., & Kassim, N. E. 2000, ApJ, 543, 611
- Paterson, A. R. 1983, A First Course in Fluid Dynamics (Cambridge: Cambridge Univ. Press), 302
- Peterson, J. R. et al. 2001, A&A, 365, L104
- Quilis, V., Bower, R. G., & Balogh, M. L. 2001, MNRAS, 328, 1091
- Reiprich, T. H. 2001, Ph.D thesis, Ludwig-Maximilians-Universität München
- Ricker, P. M., & Sarazin, C. L. 2001, ApJ, 561, 621
- Rizza, E., Loken, C., Bliton, M., Roettiger, K., Burns, J. O., & Owen, F. N. 2000, AJ, 119, 21
- Röttgering, H., Wieringa, M., Hunstead, R., & Ekers, R. 1997, MNRAS, 290, 577
- Sarazin, C. L. 1986, Rev. Mod. Phys., 58, 1
- Sarazin, C. L. 2001, in Merging Processes in Clusters of Galaxies, ed. Feretti, L., Gioia, I. M., & Giovannini, G. (Dordrecht; Kluwer), in press
- Schmidt, R. W., Allen, S. W., & Fabian, A. C. 2001, MNRAS, 327, 1057
- Slee, O. B., & Reynolds, J. E. 1984, Proc. Astron. Soc. Australia, 5, 516
- Slee, O. B., Roy, A. L. Murgia, M. Andernach, H. Ehle, M. 2001, AJ, 122, 1172
- Stark, A. A., Gammie, C. F., Wilson, R. W., Bally, J., Linke, R. A., Heiles, C., & Hurwitz, M. 1992, ApJS, 79, 77
- Sun, M., Murray, S. S., Markevitch, M., & Vikhlinin, A. 2002, ApJ, 565, 867
- Tamura, T. et al. 2001, A&A, 365, L87
- Taylor, G. B., Barton, E. J., & Ge, J. 1994, AJ, 107, 1942

- Vikhlinin, A., Markevitch, M., & Murray, S. S. 2001a, *ApJ*, 549, L47
- Vikhlinin, A., Markevitch, M., & Murray, S. S. 2001b, *ApJ*, 551, 160
- Way, M. J., Quintana, H., & Infante, L. 1997, *AJ*, submitted (astro-ph/9709036)
- White, D. A., Jones, C., & Forman, W. 1997, *MNRAS*, 292, 419
- Young, A. J., Wilson, A. S., & Mundell, C. G. 2002, *ApJ*, submitted (astro-ph/0202504)

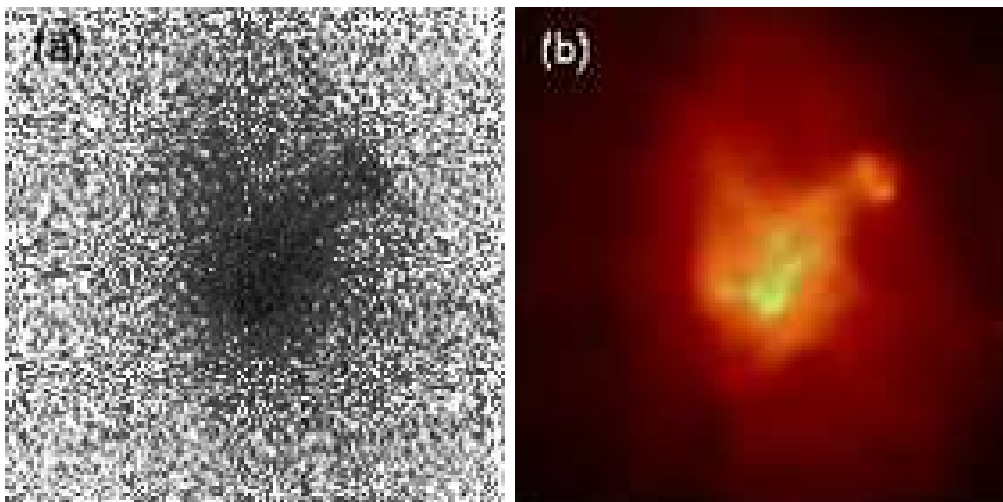


Fig. 1.— (a) Raw *Chandra* X-ray image (0.3–10 keV) of the inner $2' \times 2'$ region of Abell 133, uncorrected for exposure or background. North is up and East is left. The image pixels are $0''.492$ square. (b) Adaptively smoothed *Chandra* X-ray image of the same region, corrected for background, exposure, and vignetting.

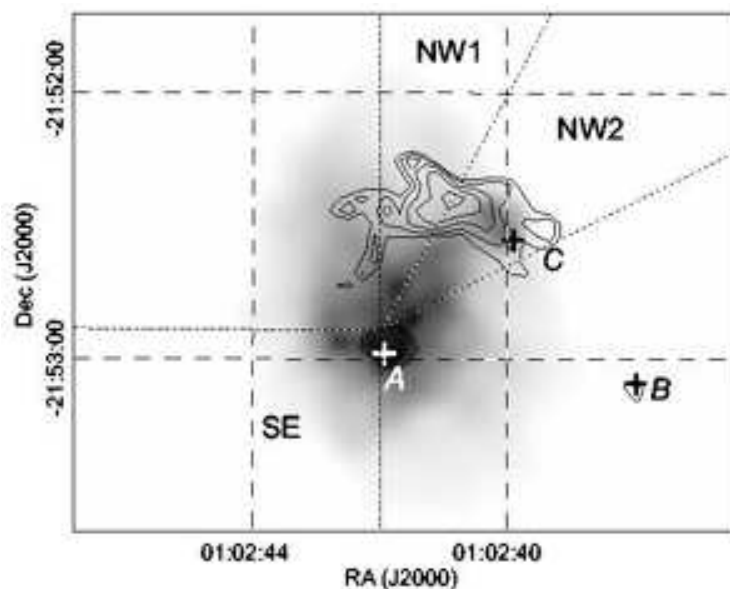


Fig. 2.— Radio brightness contours (Slee et al. 2001) overlaid on the adaptively smoothed image of the central region of Abell 133; the radio contours are logarithmically spaced by a factor of $\sqrt{2}$. The positions of several candidate X-ray point sources (A, B, C) are marked with crosses. The dotted lines show sectors (SE, NW1, NW2) used to derive X-ray surface brightness profiles.

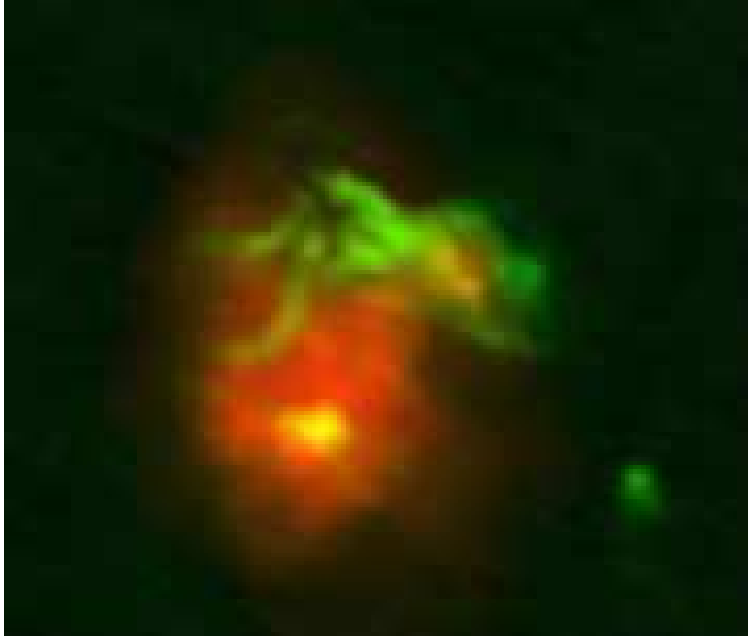


Fig. 3.— Radio image at 1.4 GHz (Slee et al. 2001) is overlaid in green on the adaptively smoothed image of the central region of Abell 133 (Fig. 1b) in red. North is up and east is left. The region covered is roughly $2' \times 1'.7$.

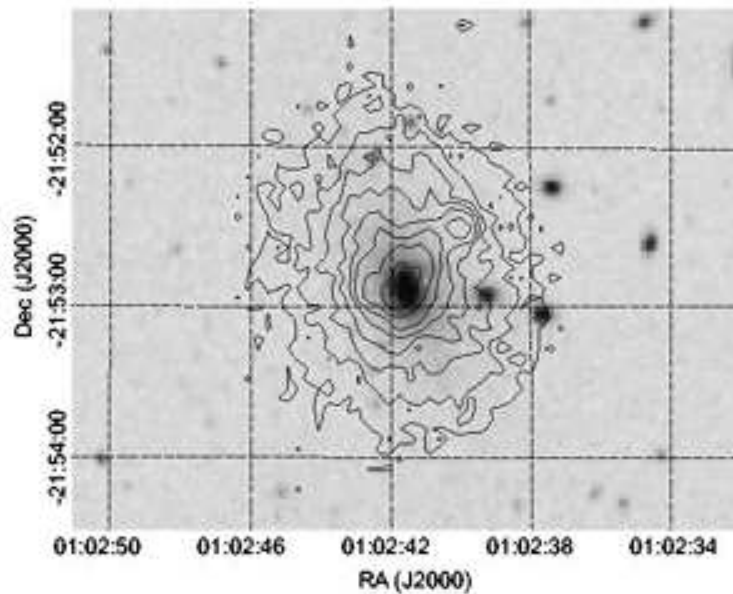


Fig. 4.— X-ray brightness contours (0.3 – 10 keV band, logarithmically spaced by a factor of $\sqrt{2}$), overlaid on the DSS optical image scanned from a SERC-J survey plate taken in 1997 at the UK Schmidt telescope, Australia.

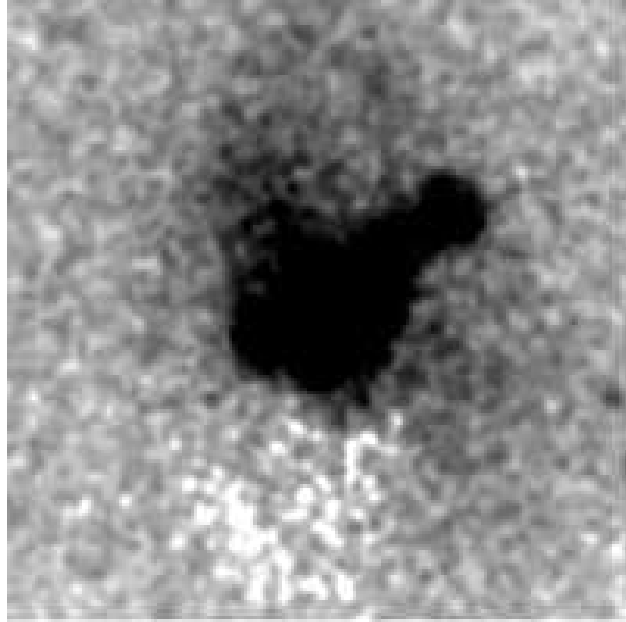


Fig. 5.— The residual emission from the central region of Abell 133 after subtracting a smooth, elliptical isophotal model. The image has been smoothed with a gaussian of $\sigma = 1''$. North is up and east is left. The image covers $2' \times 2'$.

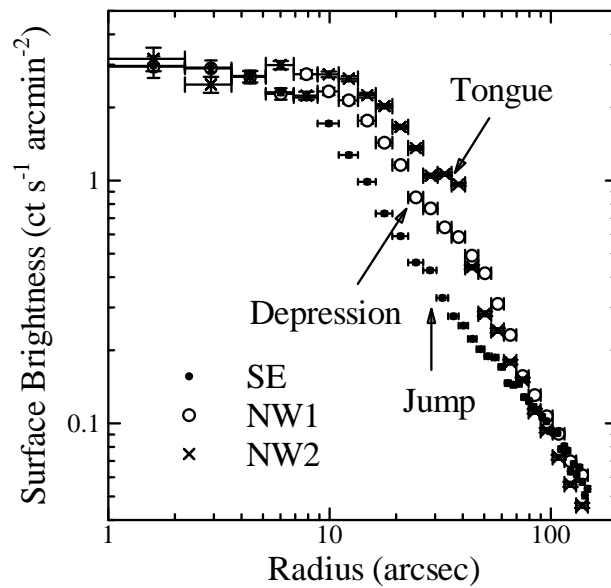


Fig. 6.— Surface brightness as a function of radius for the three sectors shown by dotted lines in Figure 2. Error bars are 1- σ Poisson uncertainties, but they are small and difficult to see except in the inner region.

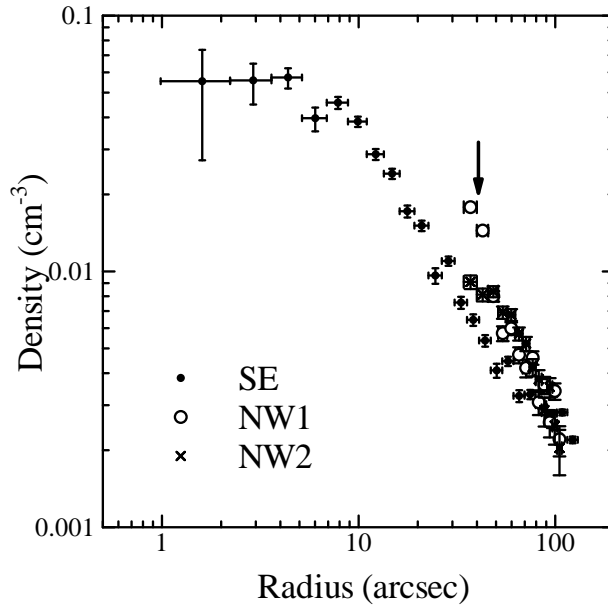


Fig. 7.— Electron density as a function of radius for the sectors shown by dotted lines in Figure 2. For NW1 and NW2 sectors, we excluded the region of the tip of the tongue (the radius of which is indicated by the arrow). Error bars are $1\text{-}\sigma$.



Fig. 8.— X-ray color image of the central region of Abell 133, produced by assigning red, green, and blue to the 0.3 – 1.5, 1.5 – 2.5, and 2.5 – 10 keV band, respectively. Thus, red regions have unusually soft X-ray emission, while green-blue regions have unusually hard emission. North is up and east is left. The image covers $2' \times 2'$.

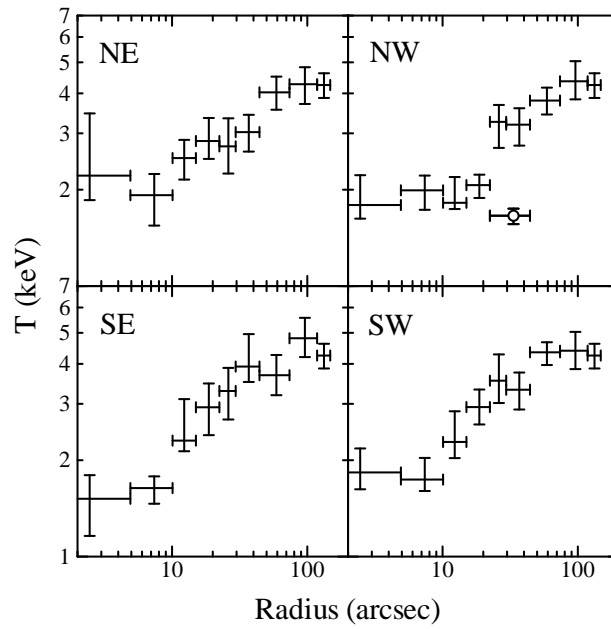


Fig. 9.— Temperature as a function of radius for the four sectors. For the NW sector, the temperatures do not include the tongue; the temperature of the tongue is shown separately by an open circle. The error bars are 90% confidence intervals.

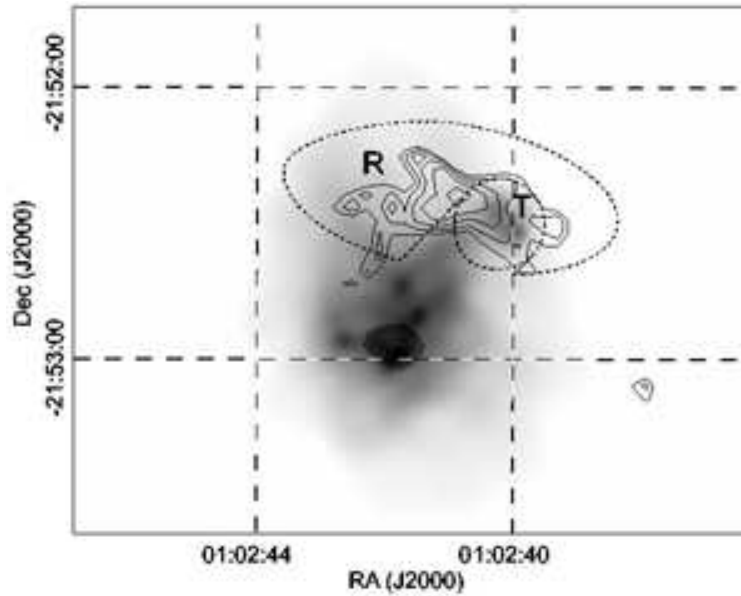


Fig. 10.— Regions for spectral analysis. The area is the same as Figure 2 but the radio relic and tongue regions are shown by dotted curves and labeled R and T, respectively.

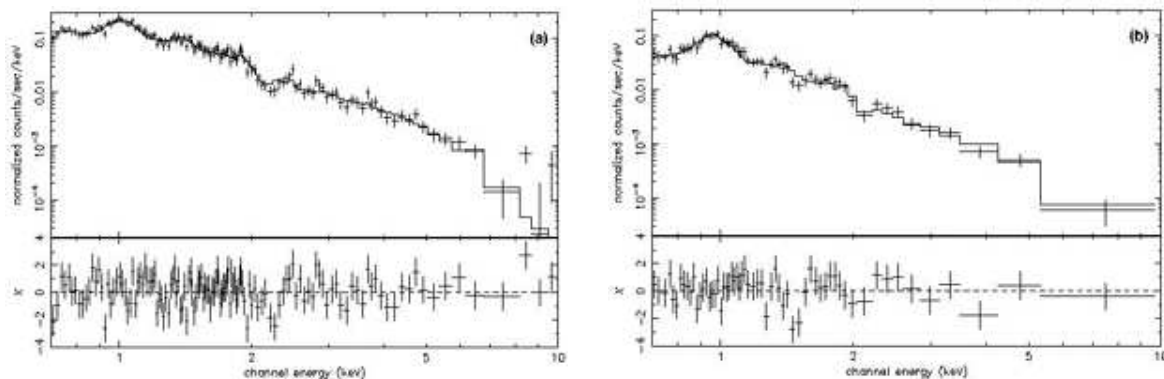


Fig. 11.— (a) The upper panel shows the X-ray spectral data and best-fit 1TPL model for the radio relic region, while the lower panel plots the residuals divided by the $1\text{-}\sigma$ errors. (b) Same as (a), but the spectrum is for the X-ray tongue region, and the best-fit model is 2T'.

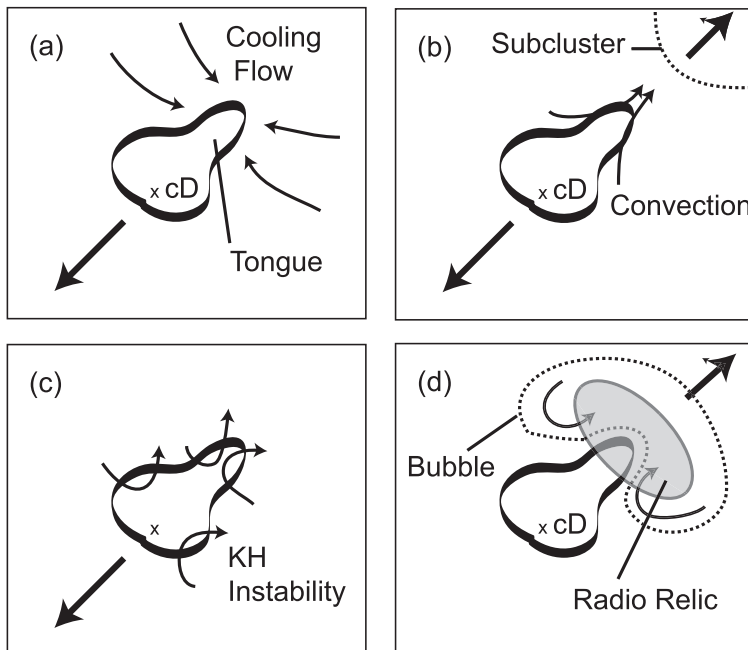


Fig. 12.— Schematic drawing of possible origins of the tongue: (a) a cooling wake, (b) a cluster merger, (c) Kelvin-Helmholtz instabilities, and (d) a buoyant radio bubble.

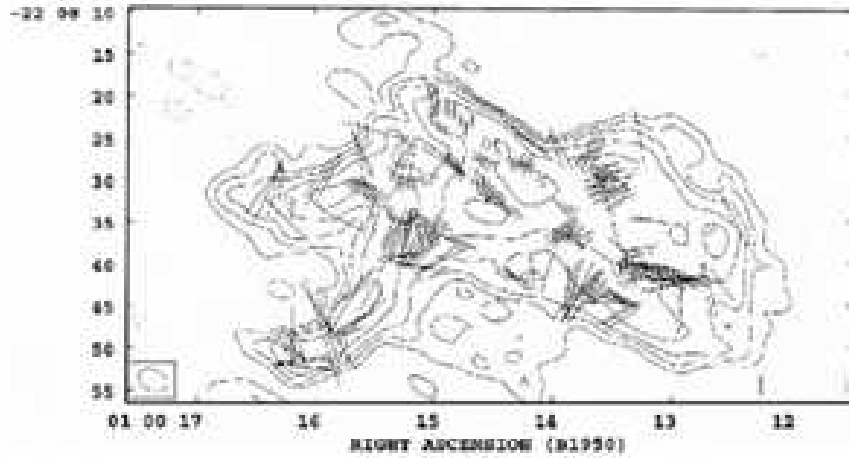


Fig. 13.— Radio polarization of the radio relic source at 1.465 GHz based on data described in Slee et al. (2001). The lines are parallel to the electric vector, and the length is proportional to the fractional polarization. The line in the rectangle at the lower right corresponds to a polarization of 10%. The contours show the radio surface brightness; the positive contours are (91, 182, 304, 607, 1214, and 2732) $\mu\text{Jy beam}^{-1}$.

Table 1. Average Spectrum of Abell 133

| Observatory | T (keV) | Z (Z_{\odot}) | N_{H} (10^{20} cm^{-2}) | $F(2 - 10 \text{ keV})$ ($10^{-11} \text{ erg cm}^{-2} \text{ s}^{-1}$) | χ^2/dof |
|----------------------|----------------------------------------|------------------------|-------------------------------------------------|------------------------------------------------------------------------------|---------------------|
| Chandra | $3.4^{+0.0}_{-0.1}$ | $0.59^{+0.04}_{-0.04}$ | $2.92^{+0.69}_{-0.63}$ | 0.75 | 452.8/315 |
| Chandra ^a | $1.4^{+0.1}_{-0.3}, 3.7^{+0.2}_{-0.2}$ | $0.59^{+0.06}_{-0.05}$ | $3.8^{+0.8}_{-0.9}$ | 0.75 | 347.1/313 |
| Einstein | $4.0^{+2.9}_{-1.4}$ | 0.5^{b} | 1.58^{c} | 1.31 | ... |
| EXOSAT | $3.8^{+2.0}_{-0.9}$ | < 1.1 | $0.28^{+0.99}_{-0.26}$ | 1.43 | 24.60/17 |

^a The ratio of the emission measure of the cold component to that of the hot component is 0.083 ± 0.035 .

^bAssumed

^cAssumed (Galactic absorption)

Table 2. Spectra for the X-ray Tongue, Radio Relic, and cD Center Regions

| Region | Model | T_1 (keV) | T_2 (keV) | Z (Z_{\odot}) | Γ | N_{H} (10^{20} cm^{-2}) | χ^2/dof |
|-----------|-------|---------------------|------------------------|------------------------------------------|---------------------|-------------------------------------------------|---------------------|
| Relic | 1T | $2.7^{+0.2}_{-0.2}$ | ... | $0.62^{+0.15}_{-0.12}$ | ... | $3.6^{+2.1}_{-1.5}$ | 156.0/128 |
| | 1TPL | $2.2^{+0.4}_{-0.2}$ | ... | 0.62^{a} | $1.7^{+0.3}_{-1.1}$ | $4.8^{+4.0}_{-3.3}$ | 147.2/127 |
| | 2T | $1.2^{+0.9}_{-0.4}$ | $2.9^{+\infty}_{-1.7}$ | $0.66^{+0.0}_{-0.30}$ | ... | $4.2^{+3.0}_{-2.8}$ | 151.1/126 |
| Tongue | 1T | $1.4^{+0.3}_{-0.0}$ | ... | $0.28^{+0.08}_{-0.06}$ | ... | $5.9^{+0.0}_{-5.9}$ | 75.8/57 |
| | 1TPL | $1.4^{+0.0}_{-0.1}$ | ... | 0.28^{a} | $0.9^{+0.6}_{-1.4}$ | $3.8^{+5.0}_{-3.8}$ | 59.1/56 |
| | 2T | $1.1^{+0.2}_{-0.2}$ | $2.3^{+1.2}_{-0.3}$ | $0.77^{+0.67}_{-0.24}$ | ... | $3.1^{+5.1}_{-3.1}$ | 52.6/55 |
| | 2T' | $1.3^{+0.0}_{-0.1}$ | 3.2^{b} | $0.66^{+0.55}_{-0.25} (0.72^{\text{b}})$ | ... | 1.3^{b} | 54.6/58 |
| cD Center | 1T | $1.7^{+0.1}_{-0.1}$ | ... | $0.42^{+0.15}_{-0.11}$ | ... | $5.4^{+4.2}_{-4.3}$ | 62.4/58 |

^aFixed at the value of 1T model.

^bFixed at the values for the ambient gas.

Table 3. Cooling Flow Spectral Fits

| r (arcsec) | T_{High} (keV) | Z (Z_{\odot}) | ΔN_{H} (10^{20} cm^{-3}) | \dot{M} ($M_{\odot} \text{ yr}^{-1}$) | χ^2/dof |
|-----------------|------------------------------------------------|------------------------------------------------------|--------------------------------------------------------|----------------------------------------------|--------------------------|
| 0 – 27 | $2.7^{+0.1}_{-0.1}$ ($2.7^{+0.1}_{-0.1}$) | $1.0^{+0.2}_{-0.1}$ ($0.85^{+0.12}_{-0.11}$) | 34^{+4}_{-5} (0^{+12}_{-0}) | 56^{+11}_{-15} (19^{+11}_{-4}) | 195.7/154 (164.1/140) |
| 27 – 45 | $3.4^{+0.2}_{-0.3}$ ($3.4^{+0.2}_{-0.3}$) | $0.78^{+0.20}_{-0.07}$ ($0.68^{+0.14}_{-0.12}$) | 28^{+6}_{-7} (0^{+15}_{-0}) | 22^{+9}_{-7} (9^{+6}_{-4}) | 178.2/136 (154.5/127) |
| 45 – 150 | $4.7^{+0.6}_{-0.5}$ ($4.7^{+0.3}_{-1.3}$) | $0.34^{+0.11}_{-0.11}$ ($0.35^{+0.15}_{-0.12}$) | 25^{+35}_{-9} ($29^{+>100}_{-29}$) ^a | 8^{+6}_{-2} (8^{+13}_{-8}) | 227.5/224 (215.3/210) |

Note. — Parenthesis show the values when the photon data below 0.9 keV are ignored.

^aCannot be constrained.

Table 4. Parameters for the KH Instability

| Clusters | T_2 (keV) | r_2 (kpc) | D | U_{KH} (km s^{-1}) | U_{obs} (km s^{-1}) | t_{KH} (10^8 yr) | T_1 (keV) | r_{max} (Mpc) | t_{cross} (10^8 yr) | $t_{\text{cross}}/t_{\text{KH}}$ |
|-----------------|----------------|----------------|-------|-------------------------------------------|--------------------------------------------|------------------------------------------|-------------------|---------------------------|---------------------------------------------|----------------------------------|
| Abell 133 | 1.4 | 25 | < 2.5 | < 380 | ... | < 1.4 ^a | 4.0 ^c | > 0.33 ^a | > 8.4 ^a | > 6.0 ^a |
| Abell 2142 | 7 | 250 | 2 | 720 | 900 | 5.8 | 9.4 ^c | 0.57 | 6.2 | 1.1 |
| Abell 3667 | 4 | 400 | 3.9 | 850 | 1400 | 6.9 | 6.5 ^c | 0.66 | 4.6 | 0.67 |
| RX J1720.1+2638 | 6 | 200 | 2 | 670 | 500 | 8.3 | 5.6 ^d | 0.40 | 7.8 | 0.94 |
| MS 1455.0+2232 | 5 | 200 | 2.7 | 760 | ... | > 5.8 ^b | 4.8 ^e | < 0.42 ^b | < 5.3 ^b | < 0.91 ^b |
| 1E0657–56 | 7 | 25 | 3.8 | 1100 | 3500 | 0.2 | 14.8 ^f | 2.1 | 5.9 | 30 |

^a $U_{\text{obs}} > 380 \text{ km s}^{-1}$ is assumed.

^b $U_{\text{obs}} < 760 \text{ km s}^{-1}$ is assumed.

^cDavid et al. (1993)

^dMazzotta et al. (2001)

^eMazzotta et al. (2002c)

^fMarkevitch et al. (2002)